Article

Spontaneous travelling cortical waves gate perception in behaving primates

Zachary W. Davis[1,7 ✉], Lyle Muller[1,2,3,4,7], Julio Martinez-Trujillo[3,5,6], Terrence Sejnowski[1] & John H. Reynolds[1 ✉]

Perceptual sensitivity varies from moment to moment. One potential source of this variability is spontaneous fluctuations in cortical activity that can travel as waves[1]. Spontaneous travelling waves have been reported during anaesthesia[2–7], but it is not known whether they have a role during waking perception. Here, using newly developed analytic techniques to characterize the moment-to-moment dynamics of noisy multielectrode data, we identify spontaneous waves of activity in the extrastriate visual cortex of awake, behaving marmosets (*Callithrix jacchus*). In monkeys trained to detect faint visual targets, the timing and position of spontaneous travelling waves before target onset predicted the magnitude of target-evoked activity and the likelihood of target detection. By contrast, spatially disorganized fluctuations of neural activity were much less predictive. These results reveal an important role for spontaneous travelling waves in sensory processing through the modulation of neural and perceptual sensitivity.

Our perceptual experience can be highly variable. A faint stimulus presented at perceptual threshold may be detected in one instance but go undetected at another time. Cortical neurons emit variable spike patterns in response to repeated presentations of an identical stimulus[8,9]. This variability is partly a result of ongoing spontaneous fluctuations in the local network state that regularly show periods of high or low excitability[10–12] and are reflected in the local field potential (LFP)[13,14]. Spontaneous fluctuations have been observed to propagate in a wave-like fashion in visual[2,4,5,7], auditory[6] and somatosensory[3] cortex under anaesthesia, but only in slow-wave fluctuations associated with sleep or low arousal. Therefore, it remains unresolved whether waking spontaneous fluctuations travel as waves and, if they do, whether they contribute meaningfully to waking cortical function[15]. In this study we report that moment-by-moment fluctuations of neural activity recorded in behaving, non-human primates propagate as waves across the extrastriate middle temporal (MT) visual area and strongly influence spontaneous spike rates. Critically, these waves are generated endogenously, without requiring an external event to trigger them. They are thus an internally generated brain state, distinct from sensory- and behaviour-evoked waves[5,16–19]. Furthermore, we find that spontaneous waves strongly regulate visual perception. In particular, in the excitable phase of a travelling wave, both target-evoked neuronal responses and perceptual sensitivity are elevated in monkeys performing a challenging visual detection task.

We chronically implanted multi-electrode arrays (Utah Arrays, Blackrock Microsystems) into the motion-selective visual area MT of two marmosets. The structure and small size of the lissencephalic cortex enabled us to record simultaneously from the majority of the cortical area (Fig. 1a, b). We measured receptive fields of well isolated neurons and multi-unit activity in these monkeys as they maintained fixation (Extended Data Fig. 1). We also examined LFPs, which are driven by synaptic currents in the vicinity of the electrode and reflect the activity within the local network[10,13,14]. From the perspective of a single electrode, the raw LFP spontaneously fluctuated with broad spectral energy[20]. However, these fluctuations were not synchronous across the cortical area. Rather, the peak of a fluctuation often moved coherently with the spatiotemporal profile of a travelling wave (Fig. 1b, Supplementary Video 1). Peaks and troughs in the LFP have been found to correspond to epochs of relatively low and high excitability in the local network[14]. We hypothesized that, when organized as waves, these excitability states might gate the flow of spiking activity through cortical circuits, depending on their alignment (Fig. 1c).

Reliably detecting spontaneous waves in noisy multichannel data is challenging. Many wave-detection techniques rely on spike-triggered averaging[5], spatial smoothing[4] or narrowband temporal filtering[16,19,21], which can distort phase estimations of the underlying veridical fluctuation, giving false positives or unreliable measures of wave dynamics. Furthermore, unlike during anaesthesia, waking cortical dynamics are more complex, dominated by higher frequency, lower amplitude fluctuations that are more variable across the cortex[22,23]. To address this, we adapted a recently introduced statistical method for detecting travelling waves in noisy multichannel data[24] that is better suited to studying the dynamics of awake cortex (Extended Data Fig. 2). This method uses LFP phase to detect coherent flows of activity. However, whereas phase is conventionally analysed only for narrowband oscillations, such as the theta (4–8 Hz) and alpha (8–13 Hz) frequency bands[25–27], the network fluctuations we observed were not stable, sustained narrowband oscillations[20] (Fig. 2b). Rather, they were broad in frequency content, which shifted from moment to moment.

[1]The Salk Institute for Biological Studies, La Jolla, CA, USA. [2]Department of Applied Mathematics, Western University, London, Ontario, Canada. [3]Robarts Research and Brain and Mind Institute, Western University, London, Ontario, Canada. [4]Institut de Neurosciences de la Timone (INT), UMR7289, CNRS, Aix-Marseille Université, Marseille, France. [5]Department of Physiology and Pharmacology, Schulich School of Medicine and Dentistry, Western University, London, Ontario, Canada. [6]Department of Psychiatry, Schulich School of Medicine and Dentistry, Western University, London, Ontario, Canada. [7]These authors contributed equally: Zachary W. Davis, Lyle Muller. ✉e-mail: zdavis@salk.edu; reynolds@salk.edu
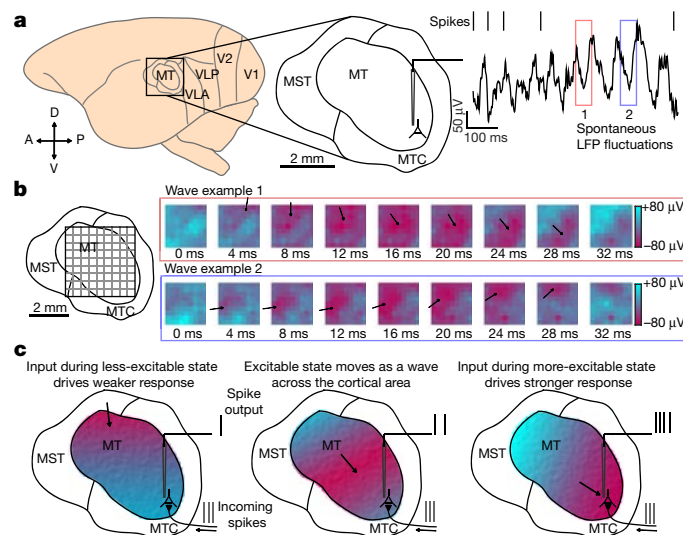
Fig. 1 | Spontaneous LFP fluctuations often travel as waves across the cortex. a, Recordings were made from visual area MT of the common marmoset. The raw (1–100 Hz) LFP recorded from a single electrode was spectrally complex, with large, dynamic spontaneous fluctuations (red and blue boxes). **b**, When viewed simultaneously across a multielectrode array, spontaneous fluctuations in the wideband (5–40 Hz) LFP often travelled as a wave (example waves from red and blue boxes). The peaks and troughs of the wave corresponded to spatially distinct regions of cortex that were in more-excitable (red) or less-excitable (blue) states. **c**, Our mechanistic hypothesis: as waves traverse cortex, they alter excitability states, modulating the relative spiking output on the basis of their alignment, with the more-excitable (red) and less-excitable (blue) phases momentarily potentiating and reducing sensitivity to incoming spikes. A, anterior; P, posterior; D, dorsal; V, ventral; MST, medial superior temporal; MTC, medial temporal cortex; VLA, ventrolateral anterior area; VLP, ventrolateral posterior area.

Fig. 2 | Spontaneous travelling waves modulate ongoing spiking probability. a, Illustration of the GP measure. The GP (coded by colour) describes the phase of the dominant fluctuation in the wideband (5–40 Hz, coloured line) LFP at each moment, and matched well to the raw LFP (5–200 Hz, black line). **b**, Power spectral density for the raw, unfiltered LFP in **a** (black line) and 20 additional single trials in grey (5–40 Hz marked by black dashed lines). **c**, Blue bars indicate the relative frequency of spikes across GPs, peaking near $\pm\pi$ rad (number of spikes > 1.5×10^5; Rayleigh test, $P < 1 \times 10^{-5}$; example from monkey W). There is no phase relationship when the LFP is averaged across electrodes (red dots). **d**, Scatter plot showing phase offsets with distance from the putative source of a detected spontaneous wave (black dots). The slope of the linear fit (red line) corresponds to the speed of the wave. The grey lines show the fits for multiple spatial shuffles. **e**, Spontaneous fluctuations had varying degrees of wave organization ($\rho_{\phi,d}$, black line). Similarly filtered randomly generated noise does not exhibit wave organization (grey line; 99% cut-off of noise distribution, dashed line; example wave correlation value, red line).

To track these fluctuating patterns, we developed a technique for computing the generalized phase (GP) of the wideband filtered (5–40 Hz) LFP (Fig. 2a). The wide frequency band captured the dominant fluctuating components of the LFP while excluding (1) the lowest frequencies that are thought to reflect slow global changes such as arousal[23,28] and (2) higher frequencies to avoid contamination of the LFP by spike artefacts[29]. Consistent with the identification of wave peaks and troughs as reflecting less- and more-excitable states, spontaneous spiking was strongly dependent on GP, with spike probability at the more-excitable state ($\pm\pi$ rad) approximately twice that of the less-excitable state (0 rad; monkey W, $n > 1.5 \times 10^5$ spikes across 20 recording sessions; $P < 1 \times 10^{-5}$, Rayleigh test for circular uniformity; Fig. 2c). The wide-band filter captured the waveform of the LFP better than alpha and theta narrowband filters (681 ms example LFP trace; Pearson's correlation: wideband $r = 0.91$, significantly different from alpha $r = 0.38$ and theta $r = 0.23$, $\alpha = 1 \times 10^{-5}$ confidence interval (CI) test; Extended Data Fig. 3a) and spontaneous spiking activity was more coupled to GP than the phase of theta or alpha (Extended Data Fig. 3b, c). The strong spike–GP coupling was spatially specific[13,30], as phases from adjacent electrodes were significantly less coupled to spike timing (monkey W, $P < 1 \times 10^{-4}$; monkey T, $n = 18$ sessions, $P < 1 \times 10^{-3}$; two-sided Wilcoxon signed-rank test; Extended Data Fig. 4).

Use of a wideband filter avoids phase distortions that could artificially produce waves or distort estimates of wave properties. Our wave-detection algorithm was applied to spatially unsmoothed data, thus preserving as much of the veridical relationship between phase and spatial position as possible. The strength of wave-like spatiotemporal organization acros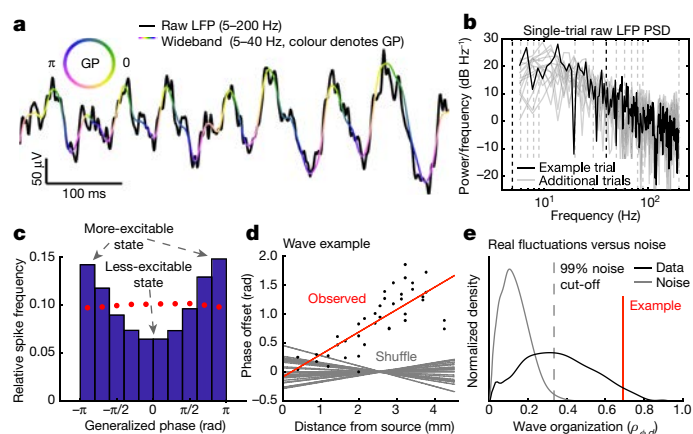s electrodes was quantified by the circular–linear correlation ($\rho_{\Phi,d}$) of GP (Φ) with distance (d) from putative sources on the recording array (Fig. 2d). $\rho_{\Phi,d}$ spans from 0 (perfectly uncorrelated random noise) to 1 (perfect radial wave organization). During spontaneous fluctuations on the Utah array, the distribution of this measure spans up to 0.8, whereas for a matched number of trials of filtered Gaussian random noise, the 99th percentile is approximately 0.3 (Fig. 2e). We then took this value as a threshold for wave-like states.

We found that spontaneous waves occurred frequently (monkey W, 11.98 ± 4.38 s^{-1}; monkey T, 9.18 ± 4.18 s^{-1} (mean ± s.d.)). Spontaneous waves travelled at speeds consistent with the conduction velocity of spikes travelling along unmyelinated horizontal projection axons (0.1–0.6 m s^{-1}; Extended Data Fig. 2d), suggesting that waves propagate via the horizontal fibres that populate the superficial and deep layers of cortex[31–33]. The average power spectrum for detected wave epochs exhibited reduced low-frequency power (<12 Hz; monkey W, $n = 215$ fixation epochs with waves and 524 epochs without waves, $P < 1 \times 10^{-4}$; monkey T, $n = 113$ epochs with wave and 938 epochs without waves, $P < 1 \times 10^{-5}$, two-sided Wilcoxon rank-sum test; Extended Data Fig. 2c) and consistent power distributed over a broad range from 10 to 30 Hz, suggesting that spontaneous waves reflect a distinct cortical state. It was not the case that larger fluctuations were more likely to be waves, as there was no difference in the amplitude distribution between wave and non-wave fluctuations (monkey W, $n = 798$ wave and 216 non-wave fluctuations, $P = 0.85$; monkey T, $n = 696$ wave and 565 non-wave fluctuations, $P = 0.79$; two-sample F-test for equal variances; Extended Data Fig. 2e). Furthermore, although previous work found that high-contrast visual stimulation attenuates waves with a spike-triggered average (STA) analysis[5], our method identified travelling waves while the monkeys freely viewed high-contrast naturalistic images (with −50 to +100 ms perisaccadic activity excluded; Extended Data Fig. 5), indicating that travelling waves are present during natural vision.
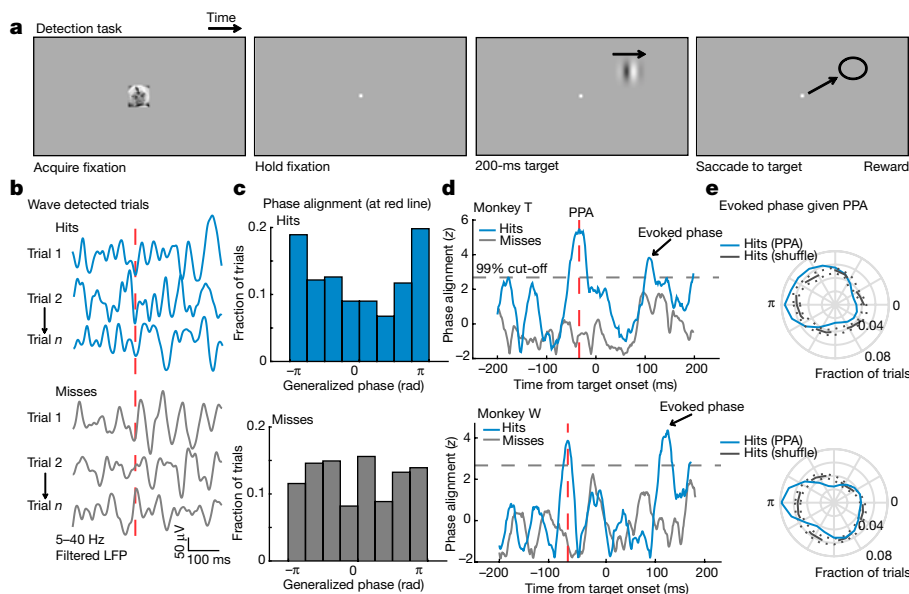
Article

Fig. 3 | Waves facilitate detection when aligned with the retinotopic location of visual targets. a, Target-detection task. A marmoset face appeared, and when foveated it was replaced with a fixation point. Marmosets held fixation until a target (200-ms drifting Gabor) appeared at one of two possible locations after a random delay. The marmoset was rewarded with juice for making a saccade to the target location. **b**, Example wideband LFP traces from a target-aligned electrode (hits, top; misses, bottom) where waves were detected on the array at the time indicated by the red-dashed line. **c**, Distributions of phase across hit (blue, top; $n = 223$ trials) and miss trials (grey, bottom; $n = 298$ trials) at the time in **b**. Data are from monkey T.

d, The cross-trial phase alignment in **c** plotted for each moment in time around the onset of the target for monkey T (top) and monkey W (bottom, $n = 348$ hits, 412 misses). Each phase distribution was z-scored relative to shuffled phase distributions (grey dashed line, 99% cut-off from permutation control). The time of peak phase alignment (red dashed line) is shown for each monkey (−33 ms, monkey T; −60 ms, monkey W). **e**, Polar plots show the network was in a more-excitable state (±π rad) at the time of target-evoked phase alignment (arrowheads) if the aligned phase occurred at the time of peak PPA (blue line; grey line is a distribution of shuffled hits).

To test whether spontaneous waves have a role in perception, we trained two marmosets to perform a simple detection task. During the task, the monkeys were required to maintain fixation while waiting for the appearance of a low-contrast (<2% Michelson contrast) 200-ms drifting Gabor target that appeared at an unpredictable time at one of two equally eccentric locations, coinciding with retinotopic locations of channels on the array (Fig. 3a). Juice reward was provided if the monkey made a saccade to the location of a target within 500 ms of target onset. For each monkey, target contrast was set to a value that was detected approximately 50% of the time (Extended Data Fig. 7a).

We hypothesized that target detection should be facilitated when spontaneous waves align a more-excitable state with target locations. To test this, we collected trials in which waves were detected (monkey W, 80.05% of trials; monkey T, 57.37%; collapsed across both target locations) and determined whether detection probability varied with the state of the wave, measured at the retinotopically aligned electrode (Fig. 3b, c). We only included trials in which fixation had been maintained for at least 300 ms before target onset to avoid including waves triggered by the saccade to fixation that initiated each trial[19]. To avoid any confounding effect owing to the activation by the target itself, we leveraged the observation that similar wave phases tend to recur over 1–2 sequential cycles[34], and examined wave alignments before the presentation of the target that predicted detection performance. Detected targets (hits) tended to be preceded by the alignment of a particular wave phase (peak was −60 ms relative to target onset for monkey W, $P < 1 \times 10^{-3}$; −33 ms for monkey T, $P < 1 \times 10^{-5}$; Rayleigh test; Fig. 3d–g). We refer to this as the pre-target phase alignment (PPA). No significant phase alignment was observed in non-wave trials (not shown).

Next, we investigated how the alignment of waves before the target appeared affected detection performance. We hypothesized that this aligned phase was predictive because it led to a more-excitable state during the target-evoked response, which favoured detection. To test

this hypothesis, we selected trials with detected waves that had a phase at the peak of PPA within ±π/6 of the aligned phase. For these trials, we computed the LFP phase during the target-evoked response. Consistent with our prediction, the target-evoked LFP was more likely to be in the more-excitable state (±π; blue trace, Fig. 3e) than expected from randomly selected hit trials (grey trace, Fig. 3e; permutation test, $\alpha = 0.01$). This indicates that PPA is indicative of waves that lead directly to a more-excitable network state during the target-evoked response.

We wanted to know whether this predictive wave alignment reflected a shift in sensitivity for faint targets, or an increase in response bias to the target location. We therefore tested whether waves were predictive of false alarms, defined as a saccade to a potential target location when no target was presented. We found no evidence that more-excitable wave states were predictive of false alarms (Extended Data Fig. 6). We therefore conclude that the alignment of spontaneous waves modulated the monkeys' sensitivity to the appearance of a faint target.

If true, the wave state should modulate the magnitude of evoked responses caused by the appearance of the target. Consistent with the observation that stronger target-evoked responses are correlated with better detection performance[35], we found that firing rates during the target-evoked response (80–200 ms from target onset) were higher for hits than misses for both monkeys (monkey W, $n = 25$ single units and 83 multi units, $P = 0.0015$; monkey T, $n = 27$ single units and 110 multi units, $P < 1 \times 10^{-5}$; two-sided Wilcoxon signed-rank test; Extended Data Fig. 7d, e). We hypothesized that the more-excitable states following PPA increased the magnitude of evoked activity, producing the stronger evoked responses correlated with improved detection. To test this, we calculated average multi-unit firing rates collapsed across target-aligned electrodes for trials in which waves were of the aligned phase, or in the opposite phase at PPA (Fig. 4a, c). Consistent with our hypothesis, the evoked firing rate was larger across units for trials in which a wave occurred and aligned the more-excitable state
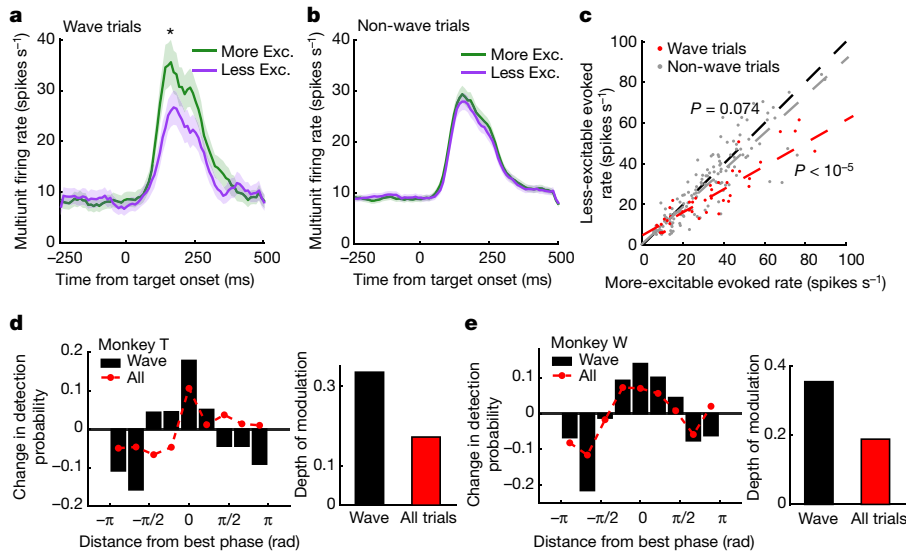
Fig. 4 | Wave state predicts target-evoked response magnitude and perceptual sensitivity. a, Average target-evoked responses following wave alignment to the more-excitable state (green line; $n = 43$ multi-units across both monkeys) were significantly greater than less-excitable wave states (purple line; $P < 10^{-5}$, two-sided Wilcoxon rank-sum test; shaded regions indicate s.e.m.). **b**, The same analysis for non-wave fluctuations showed no difference ($n = 147$ multi-units; $P = 0.074$). **c**, Scatter plot of target-evoked responses across multi-units for trials in the more-excitable (x axis) or less-excitable state (y axis) at the time of PPA for wave (red dots; linear fit, red dashed line) or non-wave trials (grey dots; linear fit, grey dashed line). **d**, **e**, Left, bar plot showing the change in detection probability centred on the aligned phase at peak PPA in each monkey (rotated to 0 radians) for detected waves. Red dots show weaker phase-dependent changes in detection probability when all trials (wave and non-wave) are combined. Right, bar plot showing the depth of modulation in detection probability given wave state is roughly double the depth for all trials (monkey T, 33% to 17%, $n = 464$ wave and 494 non-wave trials; monkey W, 35% to 19%, $n = 479$ wave and 485 non-wave trials).

to the target location rather than an oppositely aligned wave ($\pm\pi/3$ rad, $n = 43$ multi-units across both monkeys; $P < 1 \times 10^{-5}$; two-tailed Wilcoxon sign-rank test). We performed the same analysis on trials that did not meet our statistical criterion for waves (that is, non-wave trials) and found that the phase did not modulate firing rates ($n = 143$ multi-units; $P = 0.074$; Fig. 4b, c).

Finally, because the pre-target wave state predicted the magnitude of target-evoked spiking, we aimed to quantify how well the monkey's likelihood of detecting the faint target could be predicted solely on the basis of knowledge of the wave state at the time of PPA. We calculated the monkey's conditional probability of target detection as a function of phase distance from the optimally aligned wave in each monkey (rotated to 0 rad). In both monkeys, the conditional probability of detection reached a maximum for the optimal phases and a minimum for opposite phases (Fig. 4d, e), with a depth of modulation of 33% (monkey T) and 35% (monkey W) from peak to trough. When we took the perspective of a single electrode, with no knowledge about the state of the wave, there remained a strong, but significantly lower phase-dependent probability of detection (17% monkey T, 19% monkey W; CI test, $\alpha = 0.05$).

Next, to quantify how wave state compared relative to other indicators of network state that have previously been found to be predictive of perceptual performance, we constructed a generalized linear model (GLM) regressing perceptual performance (hit, miss) against target-evoked spike rate[35,36], pre-target baseline activity, a measure of attentional state[37], pupillary diameter, a measure of arousal[28,38,39] and pre-target alpha power[40] (logit link function, binomial error distribution, $n = 1,277$ trials; Supplementary Table 1). On trials in which waves were detected, GP at the time of PPA was the strongest predictor of perceptual performance (GLM weight for GP, $\beta_{GP} = 0.25$, $P < 0.0001$) compared with arousal (GLM weight for pupil diameter, $\beta_{PUP} = 0.15$, $P < 0.05$) and target-evoked spiking activity (GLM weight for firing rate, $\beta_{FR} = 0.13$, $P < 0.05$). Pre-target alpha power and spontaneous pre-target firing rate were not significant predictors ($P = 0.69$ and $P = 0.80$, respectively).

Together, these results demonstrate that spontaneous travelling waves occur in the neocortex of the awake monkey, and that they modulate sensory-evoked responses and gate perception. The waves travel at speeds consistent with the conduction velocity of unmyelinated horizontal axons that populate the superficial and deep layers of cortex, suggesting that they emerge from the activation of cortical populations by spikes travelling along topographic connections that fall off with distance. These waves are distinct from the large, slow-wave deflections reported during anaesthesia or quiet wakefulness[41,42]. Rather, they are present during active vision, and their alignment preceding the presentation of a target predicts detection performance. Notably, these wave effects are only apparent because of our measurement of the GP, and cannot be explained by latent narrowband oscillations embedded in the wideband signal. Narrowband filtering in alpha or beta bands fails to reveal any phase alignment predictive of perception (Extended Data Fig. 8), and GP provides a better estimate of perceptual state than instantaneous voltage amplitude (Extended Data Fig. 9).

The importance of waves to perception is further underscored by the fact that they are more predictive of perceptual sensitivity than previous reports of pre-target alpha-oscillation phase in visual detection[43–45] or theta-oscillation phase in frontal-parietal networks during the deployment of attention[46,47]. We speculate, given that we observe weaker predictive effects when we mix wave and non-wave trials, that the alpha and theta effects previously observed were in fact due to the undetected presence of travelling waves. This is supported by the recent discovery that alpha and theta oscillations travel as propagating waves across awake human cortex[21]. If these two phenomena are related, this raises the possibility that spontaneous waves may also be coordinated across brain areas. Such coordination might explain how waves in MT are so strongly predictive of detection for stimuli that presumably activate other visual areas such as V1. These results have important implications for the neural organization of sensory processing and demonstrate that, when viewed across the spatial extent of the cortex, fluctuations of cortical activity are neither purely synchronous nor spatially disorganized noise processes. Rather, neocortex exhibits

Article

propagating waves of activity that dynamically regulate neuronal responses and perceptual sensitivity.

GLM analysis

To determine the relative predictive power of the state of spontaneous travelling waves compared to other measures of network state on the detection task, we fitted a GLM to the trial-by-trial responses of the monkeys. Predictors included (1) target-evoked firing rate, measured from +80 to +200 ms after target onset, (2) the attentive state, estimated by the spontaneous spike rate measured during a window preceding the appearance of the target (−120 to 0 ms), (3) the pre-target alpha (8–13 Hz) power 50 ms before target onset, measured as the instantaneous power (Hilbert transform modulus) after narrowband filtering and normalized by the broadband power spectrum (5–200 Hz), (4) arousal state, estimated by the pupil diameter at the time of target onset, and (5) GP at the time of maximal PPA (Fig. 3f). For the measure of normalized alpha-band power, transformation by the logarithm function was used for the purpose of variance stabilization. The fit was performed using 1,277 trials on which waves were detected in both monkeys. Predictor distributions were standardized by z-scoring before fitting so that resulting model weights (β_{FR}, β_{SP}, β_{α}, β_{PUP}, β_{GP}) could be compared to assess relative importance[60,61]. The GLM was fitted using a logit link function to relate changes in the continuous predictor variables to the binary response variable (hit or miss in the detection task). Individual predictors were evaluated by calculating the t-statistic associated with the estimated weight ($H_0: \beta = 0, H_1: \beta \neq 0$), with significance determined at the $\alpha = 0.05$ level.

Reporting summary

Further information on research design is available in the Nature Research Reporting Summary linked to this paper.

Online content

Any methods, additional references, Nature Research reporting summaries, source data, extended data, supplementary information, acknowledgements, peer review information; details of author contributions and competing interests; and statements of data and code availability are available at https://doi.org/10.1038/s41586-020-2802-y.

1. Engel, T. A. & Steinmetz, N. A. New perspectives on dimensionality and variability from large-scale cortical dynamics. *Curr. Opin. Neurobiol.* **58**, 181–190 (2019).
2. Roland, P. E. et al. Cortical feedback depolarization waves: a mechanism of top-down influence on early visual areas. *Proc. Natl Acad. Sci. USA* **103**, 12586–12591 (2006).
3. Ferezou, I., Bolea, S. & Petersen, C. C. H. Visualizing the cortical representation of whisker touch: voltage-sensitive dye imaging in freely moving mice. *Neuron* **50**, 617–629 (2006).
4. Xu, W., Huang, X., Takagaki, K. & Wu, J.-Y. Compression and reflection of visually evoked cortical waves. *Neuron* **55**, 119–129 (2007).
5. Nauhaus, I., Busse, L., Carandini, M. & Ringach, D. L. Stimulus contrast modulates functional connectivity in visual cortex. *Nat. Neurosci.* **12**, 70–76 (2009).
6. Reimer, A., Hubka, P., Engel, A. K. & Kral, A. Fast propagating waves within the rodent auditory cortex. *Cereb. Cortex* **21**, 166–177 (2011).
7. Townsend, R. G. et al. Emergence of complex wave patterns in primate cerebral cortex. *J. Neurosci.* **35**, 4657–4662 (2015).
8. Tomko, G. J. & Crapper, D. R. Neuronal variability: non-stationary responses to identical visual stimuli. *Brain Res.* **79**, 405–418 (1974).
9. Shadlen, M. N. & Newsome, W. T. The variable discharge of cortical neurons: implications for connectivity, computation, and information coding. *J. Neurosci.* **18**, 3870–3896 (1998).
10. Okun, M., Naim, A. & Lampl, I. The subthreshold relation between cortical local field potential and neuronal firing unveiled by intracellular recordings in awake rats. *J. Neurosci.* **30**, 4440–4448 (2010).
11. Luczak, A., Bartho, P. & Harris, K. D. Gating of sensory input by spontaneous cortical activity. *J. Neurosci.* **33**, 1684–1695 (2013).
12. Tan, A. Y. Y., Chen, Y., Scholl, B., Seidemann, E. & Priebe, N. J. Sensory stimulation shifts visual cortex from synchronous to asynchronous states. *Nature* **509**, 226–229 (2014).
13. Katzner, S. et al. Local origin of field potentials in visual cortex. *Neuron* **61**, 35–41 (2009).
14. Buzsáki, G., Anastassiou, C. A. & Koch, C. The origin of extracellular fields and currents—EEG, ECoG, LFP and spikes. *Nat. Rev. Neurosci.* **13**, 407–420 (2012).
15. Ray, S. & Maunsell, J. H. R. Network rhythms influence the relationship between spike-triggered local field potential and functional connectivity. *J. Neurosci.* **31**, 12674–12682 (2011).
16. Rubino, D., Robbins, K. A. & Hatsopoulos, N. G. Propagating waves mediate information transfer in the motor cortex. *Nat. Neurosci.* **9**, 1549–1557 (2006).
17. Benucci, A., Frazor, R. A. & Carandini, M. Standing waves and traveling waves distinguish two circuits in visual cortex. *Neuron* **55**, 103–117 (2007).
18. Muller, L., Reynaud, A., Chavane, F. & Destexhe, A. The stimulus-evoked population response in visual cortex of awake monkey is a propagating wave. *Nat. Commun.* **5**, 3675 (2014).
19. Zanos, T. P., Mineault, P. J., Nasiotis, K. T., Guitton, D. & Pack, C. C. A sensorimotor role for traveling waves in primate visual cortex. *Neuron* **85**, 615–627 (2015).
20. Bullock, T. H., Mcclune, M. C. & Enright, J. T. Are the electroencephalograms mainly rhythmic? Assessment of periodicity in wide-band time series. *Neuroscience* **121**, 233–252 (2003).
21. Zhang, H., Watrous, A. J., Patel, A. & Jacobs, J. Theta and alpha oscillations are traveling waves in the human neocortex. *Neuron* **98**, 1269–1281 (2018).
22. Steriade, M., Nuñez, A. & Amzica, F. A novel slow (<1 Hz) oscillation of neocortical neurons in vivo: depolarizing and hyperpolarizing components. *J. Neurosci.* **13**, 3252–3265 (1993).
23. Steriade, M., Timofeev, I. & Grenier, F. Natural waking and sleep states: a view from inside neocortical neurons. *J. Neurophysiol.* **85**, 1969–1985 (2001).
24. Muller, L. et al. Rotating waves during human sleep spindles organize global patterns of activity that repeat precisely through the night. *eLife* **5**, e17267 (2016).
25. Buzsáki, G. & Draguhn, A. Neuronal oscillations in cortical networks. *Science* **304**, 1926–1929 (2004).
26. Kayser, C., Montemurro, M. A., Logothetis, N. K. & Panzeri, S. Spike-phase coding boosts and stabilizes information carried by spatial and temporal spike patterns. *Neuron* **61**, 597–608 (2009).
27. Lopour, B. A., Tavassoli, A., Fried, I. & Ringach, D. L. Coding of information in the phase of local field potentials within human medial temporal lobe. *Neuron* **79**, 594–606 (2013).
28. McGinley, M. J., David, S. V. & McCormick, D. A. Cortical membrane potential signature of optimal states for sensory signal detection. *Neuron* **87**, 179–192 (2015).
29. Zanos, T. P., Mineault, P. J. & Pack, C. C. Removal of spurious correlations between spikes and local field potentials. *J. Neurophysiol.* **105**, 474–486 (2011).
30. Xing, D., Yeh, C.-I. & Shapley, R. M. Spatial spread of the local field potential and its laminar variation in visual cortex. *J. Neurosci.* **29**, 11540–11549 (2009).
31. Bringuier, V., Chavane, F., Glaeser, L. & Frégnac, Y. Horizontal propagation of visual activity in the synaptic integration field of area 17 neurons. *Science* **283**, 695–699 (1999).
32. Lewis, D. A. Horizontal synaptic connections in monkey prefrontal cortex: an in vitro electrophysiological study. *Cereb. Cortex* **10**, 82–92 (2000).
33. Girard, P., Hupé, J. M. & Bullier, J. Feedforward and feedback connections between areas V1 and V2 of the monkey have similar rapid conduction velocities. *J. Neurophysiol.* **85**, 1328–1331 (2001).
34. Alexander, D. M., Ball, T., Schulze-Bonhage, A. & van Leeuwen, C. Large-scale cortical travelling waves predict localized future cortical signals. *PLOS Comput. Biol.* **15**, e1007316 (2019).
35. van Vugt, B. et al. The threshold for conscious report: Signal loss and response bias in visual and frontal cortex. *Science* **360**, 537–542 (2018).
36. Palmer, C., Cheng, S.-Y. & Seidemann, E. Linking neuronal and behavioral performance in a reaction-time visual detection task. *J. Neurosci.* **27**, 8122–8137 (2007).
37. Luck, S. J., Chelazzi, L., Hillyard, S. A. & Desimone, R. Neural mechanisms of spatial selective attention in areas V1, V2, and V4 of macaque visual cortex. *J. Neurophysiol.* **77**, 24–42 (1997).
38. Niell, C. M. & Stryker, M. P. Modulation of visual responses by behavioral state in mouse visual cortex. *Neuron* **65**, 472–479 (2010).
39. Stringer, C. et al. Spontaneous behaviors drive multidimensional, brainwide activity. *Science* **364**, eaav7893 (2019).
40. Brüers, S. & VanRullen, R. Alpha power modulates perception independently of endogenous factors. *Front. Neurosci.* **12**, 279 (2018).
41. Petersen, C. C. H., Hahn, T. T. G., Mehta, M., Grinvald, A. & Sakmann, B. Interaction of sensory responses with spontaneous depolarization in layer 2/3 barrel cortex. *Proc. Natl Acad. Sci. USA* **100**, 13638–13643 (2003).
42. Poulet, J. F. A. & Petersen, C. C. H. Internal brain state regulates membrane potential synchrony in barrel cortex of behaving mice. *Nature* **454**, 881–885 (2008).
43. Busch, N. A., Dubois, J. & VanRullen, R. The phase of ongoing EEG oscillations predicts visual perception. *J. Neurosci.* **29**, 7869–7876 (2009).
44. Mathewson, K. E., Gratton, G., Fabiani, M., Beck, D. M. & Ro, T. To see or not to see: prestimulus α phase predicts visual awareness. *J. Neurosci.* **29**, 2725–2732 (2009).
45. Samaha, J., Gosseries, O. & Postle, B. R. Distinct oscillatory frequencies underlie excitability of human occipital and parietal cortex. *J. Neurosci.* **37**, 2824–2833 (2017).
46. Helfrich, R. F. et al. Neural mechanisms of sustained attention are rhythmic. *Neuron* **99**, 854–865 (2018).
47. Fiebelkorn, I. C., Pinsk, M. A. & Kastner, S. A dynamic interplay within the frontoparietal network underlies rhythmic spatial attention. *Neuron* **99**, 842–853 (2018).

Methods

Surgeries

Two marmosets (*C. jacchus*), one male (monkey W, five years of age) and one female (monkey T, three years of age) participated in this study. The sample size was chosen to minimize animal use while providing for reproducibility of results; no statistical methods were used to predetermine sample size. No blinding or randomization was applied. Each marmoset was fitted with a headpost for head stabilization and eye tracking. The headpost contained a hollow chamber housing an Omnetics connector for a Utah array, which was chronically implanted in a subsequent surgery. For this surgery, a 7 × 10 mm craniotomy was made over area MT (stereotaxic coordinates 2 mm anterior, 12 mm dorsal). An 8 × 8 (64 channel, monkey W) and 9 × 9 with alternating channels removed (40 channel, monkey T) Utah array was chronically implanted over area MT using a pneumatic inserter wand. The electrodes spacing was 400 μM with a pitch depth of 1.5 mm. The craniotomy was closed with Duraseal (Integra Life Sciences, monkey W) or Duragen (Integra Life Sciences, monkey T), and covered with a titanium mesh embedded in dental acrylic. All surgical procedures were performed with the monkeys under general anaesthesia in an aseptic environment in compliance with NIH guidelines. All experimental methods were approved by the Institutional Animal Care and Use Committee (IACUC) of the Salk Institute for Biological Studies and conformed to NIH guidelines.

Data acquisition

Marmosets were trained to enter a custom-built marmoset chair that was placed inside a Faraday box with an LCD monitor (ASUS VG248QE) at a distance of 40 cm. The monitor was set to a refresh rate of 100 Hz and gamma corrected with a mean grey luminance of 75 cds m⁻². Electrode voltages were recorded from the Utah arrays using two Intan RHD2132 amplifiers connected to an Intan RHD2000 USB interface board. Data were sampled at 30 kHz from all channels. The marmosets were headfixed by a headpost for all recordings. Eye position was measured with an IScan CCD infrared camera sampling eye position at 500 Hz. Stimulus presentation and behavioural control was managed through MonkeyLogic in Matlab. Digital and analogue signals were coordinated through National Instrument DAQ cards (NI PCI6621) and BNC breakout boxes (NI BNC2090A). Neural data was broken into two streams for offline processing of spikes (single-unit and multi-unit activity) and LFPs. Spike data were high-pass filtered at 500 Hz and candidate spike waveforms were defined as exceeding 4 × s.d. of a sliding 1 s window of ongoing voltage fluctuations. Artefacts were rejected if appearing synchronously (within 0.5 ms) on over a quarter of all recorded channels. Segments of data (1.5 ms) around the time of candidate spikes were selected for spike sorting using principal component analysis through the open source spike sorting software MClust in Matlab (A. D. Redish, University of Minnesota). Sorted units were classified as single- or multi-units and single units were validated by the presence of a clear refractory period in the autocorrelogram. LFP data was low-pass filtered at 300 Hz and down-sampled to 1,000 Hz.

Generalized phase

The analytic signal paradigm was originally developed by Denis Gabor in 1946[48], defining the concept of 'instantaneous frequency' and 'instantaneous phase' for non-stationary signals; however, owing to several technical limitations, the analytic signal representation is commonly used strictly in the context of signals pre-treated with a tight narrowband filter[49]. Here, we sought to address the technical limitations in the analytic signal to generalize its application beyond signals where tight narrowband filtering is appropriate. For this reason, we call our updated approach for non-stationary, wideband signals GP.

Consider a real-valued signal $x_n \in \mathbb{R}$ for $n \in [1,2,...,N_s]$, where N_s is the number of samples in one recorded trial obtained at a sampling frequency f_s. Given x_n, its analytic signal representation (X_n) is:

$$X_n = x_n + iH[x_n]$$

where i is the imaginary unit and $H[x_n]$ is the Hilbert transform (HT) of the signal x_n. This representation can be obtained by implementing the HT operator as a finite impulse response (FIR) filter in the time domain[50], or by using a single-sided Fourier transform approach[51,52]. Sinusoidal cycles appear in this representation as circular contours in the complex plane, whereas non-sinusoidal fluctuations appear as closed, quasi-circular contours. In this complex plane representation, phase is calculated numerically by the four-quadrant arctangent function.

The technical limitations in the analytic signal framework occur for two principal reasons. First, low-frequency intrusions effectively shift the representation by a complex constant, which has the critical effect of highly distorting phase angles estimated by the arctangent. As an initial step in the GP representation, then, we filter the signal within a wide bandpass (5–40 Hz; 8th-order zero-phase Butterworth filter), excluding low-frequency content. Note that this important step is distinct from narrow bandpass filtering (for example, 8–13 Hz), as this approach preserves a significant portion of the signal spectrum, thereby minimizing waveform distortion and potential artefacts due to narrowband filtering of broadband noise (Fig. 2a, Extended Data Fig. 3a). We then use the single-sided Fourier transform approach[51,52] on the wideband signal and compute phase derivatives as finite differences, which are calculated by multiplications in the complex plane[18,24,53]. Second, high-frequency intrusions appear in the analytic signal representation as complex riding cycles[53], which manifest as periods of negative frequencies in the analytic signal representation. As a secondary step in the GP representation, then, we numerically detect these complex riding cycles—namely, N_c points of negative frequency in the phase sequence Arg[X_n]—and utilize shape-preserving piecewise cubic interpolation on the next $2N_c$ points of Arg[X_n] following the detected negative frequency epoch. The resulting representation captures the phase of the largest fluctuation on the recording electrode at any moment in time (Fig. 2a), without the distortions due to the large, low-frequency intrusions or the smaller, high-frequency intrusions characteristic of the 1/f-type fluctuations in cortical LFP[54–56]. The GP represents a coherent numerical approach to the original analytic signal framework of Denis Gabor[48], suitable for implementation in modern digital signal processing applications.

Wave detection

We employed a recently introduced statistical approach to detect spontaneous travelling waves in noisy multichannel recordings[18,24], adapted to utilize GP. The advantage of GP is to capture the dominant fluctuation on each electrode at each point in time; furthermore, it does not distort the signal waveform, as would occur with a narrowband filter. When these fluctuations are shared across electrodes and exhibit consistent phase offsets, the algorithm detects these patterns as travelling waves, as described below and illustrated in Extended Data Fig. 2.

Spontaneous waves were detected during epochs of fixation, excluding 50 ms before and 100 ms after eye movements, identified from the eye tracking signals. The wave-detection technique occurs in three steps. First, the algorithm finds the time point nearest to each positive LFP peak on the array. This defines a flexible window in which we test for a spontaneous wave, where the phases are valid in a neighbourhood around that time point. Second, the algorithm finds the most likely starting point for the wave, by finding the point that maximizes the divergence of the phase gradient in a smoothed version of the scalar phase field. This captures the point from which neural activity flows outward at each moment. Third, with the putative source point found, the algorithm then quantifies how clearly activity is organized about this point, by calculating the circular-linear correlation with distance

$(\rho_{\varphi,d} \in [-1,1])$ across the whole electrode array[57], consistent with our observation that the wavelengths were long relative to the spatial extent of the array. Importantly, this step is done on the tested scalar phase field without spatial smoothing, which prevents smoothing artefacts from contaminating the results. Finally, a null distribution was constructed for $\rho_{\varphi,d}$ by randomly shuffling phase values on the electrode array. Unless stated otherwise, a scalar threshold of 0.3 was used to detect waves throughout, which represented a conservative threshold on all constructed null distributions.

Data inclusion criteria

Only visually responsive units (defined by having a mean evoked firing rate 80–200 ms after target onset that was at least 2 times the mean baseline firing rate, computed from −200 to 0 ms) were included. Units were excluded if they had fewer than 6 trials on which the preferred-orientation target appeared in the unit's receptive field on the trial type being considered (hits vs misses; wave vs non-wave). For the analysis of power spectral density in Extended Data Fig. 2c, wave trials were only included if they exhibited at least four detected waves over a 300-ms fixation epoch. For the analysis in Fig. 3e, trials were only included if a wave was detected before target onset on hit trials, and phase at the target-aligned electrode was within $\pm\pi/6$ of the aligned phase.

Receptive field mapping

Receptive fields were mapped through reverse correlation. The marmoset was trained to hold fixation on an image (marmoset face, 1° of visual angle (DVA) square) presented to the centre of the LCD monitor. A drifting Gabor (2° diameter, spatial frequency: 0.5 cycles per degree, temporal frequency 10 cycles s^{-1}) was presented at a random position on the monitor between 0–18° in azimuth and −15° to 15° in elevation, drifting in one of 8 possible directions for 200 ms, after which it disappeared. After a random delay drawn from an exponential distribution (mean 40 ms), a new probe appeared and the pattern repeated until the marmoset broke fixation (defined as an excursion of 1.5° from fixation) or viewed 16 probes. The marmoset was given a juice reward proportional to the number of probes presented. The receptive field for each unit recorded on the array was estimated by calculating the spike-triggered average (STA) stimulus that evoked the maximal response:

$$STA = \frac{1}{N} \sum_i^N x_i y_i$$

The STA is the sum of probe location x_i weighted by the spike count y_i within the time bin 40 to 200 ms after probe onset, normalized by the number of all recorded spikes N. From the location of estimated receptive fields on each spiking channel, and the known topography of area MT in the marmoset[58], we estimated the relative position of each recording array in marmoset cortex (Fig.1a). We excluded from the analysis the upper half of monkey W's array as the recordings did not appear to be in area MT.

Target detection task

Marmosets initiated each trial by fixating a marmoset face (a stimulus that naturally attracts marmoset gaze) that, upon fixation, transformed into a fixation point (0.15 DVA). They were trained to hold fixation on the fixation point (1.5° tolerance) awaiting the appearance of a drifting Gabor (4 DVA diameter which reliably produced evoked responses on 1–2 electrodes; spatial frequency, 0.5 cycles per degree; temporal frequency, 10 cycles s^{-1}, drifting in one of up to 8 possible directions). After establishing fixation, the marmoset was required to hold fixation for a minimum duration (monkey W, 400 ms; monkey T, 300 ms) to avoid contamination from waves caused by the saccade to the fixation point[19]. Early fixation breaks (defined by the excursion of the eye position from the fixation window) were excluded from analysis. The target only

appeared if fixation was held for an additional random duration drawn from an exponential distribution (mean 200 ms) to generate a flat hazard function. The target could appear at one of two locations selected based on receptive field mapping at equal eccentricity (7° monkey W, 8° monkey T). The target was presented for 200 ms, after which the monkey had 300 ms (for a total of 500 ms) to saccade to within 2.5° of the target centre for a juice reward. In 10% of trials no target was presented, and the monkey was rewarded for holding fixation to the trial end. If a saccade reached the target in less than 100 ms from target onset, the trial was rejected from analysis. The trial was classified as a miss if the marmoset broke fixation to a non-target location after the target had appeared, or if the marmoset held fixation until after the response window closed. The trial was classified as a false alarm if the monkey broke fixation to a target location after achieving a minimum fixation duration (500 ms) but when no target had been shown to any location. This minimum duration was to help avoid classifying early fixation breaks as false alarms. Only trials from the preferred directions of motion (preference defined as the difference between the mean response for a direction and the mean response to the orthogonal direction, divided by their sum; trials were excluded if preference was < 0.2) presented within the receptive field of a single- or multi-unit were analysed for that unit. The target contrast that produced a correct detection rate of 50% was selected for each monkey (mean 1.4 percent Michelson contrast for both monkeys). High-contrast (10 percent Michelson contrast) targets were presented on 10% of trials. If performance for these targets was below 70 percent, the session was rejected from analysis.

Free viewing natural images

Marmosets were headfixed and their gaze monitored as in the previous tasks. Greyscale versions of naturalistic images (spanning 20–30 DVA) were randomly interleaved and presented to the monkey. The monkey was free to look at the images, and after 10 s was given a juice reward. Saccades were identified from the absolute value of the first numerical derivative of the smoothed vertical and horizontal eye traces (5 ms sliding Gaussian). Saccades were defined as velocity peaks exceeding 25°s^{-1}. We analysed periods between saccades, excluding 50 ms before and 100 ms after each detected saccade.

Cross-trial phase alignment

To quantify alignment of the GP across trials, we used the standard formulation for the Kuramoto order parameter:

$$r = \frac{1}{N_t} \sum_j^{N_t} e^{i\phi_j}$$

where N_t is the number of trials in each condition (hit or miss), i is the complex unit, and φ_j is the GP at the tested time point. The order parameter ranges between 0 (uniform distribution of phase values) and 1 (identical phase values for each trial). To compare meaningfully between two sets of observations (hit and miss) with slightly different number of trials while accounting for the expected mean and variances of the order parameter at finite scales[59], all phase alignment values were put in z-score units of a null distribution computed from 10,000 iterations of the value from randomly selected trials, with the same number of observations.

Conditional probability estimate

In order to understand how waves modulate the probability of target detection, we calculated the conditional probability of detection at each phase:

$$p(h|\phi_i) = \frac{p(\phi_i|h)p(h)}{p(\phi_i)}$$

where $h \in \{0,1\}$ is an indicator variable for target detection and ϕ_i represents GP in bin $i \in [1, N_b]$, where N_b is the number of bins (nine throughout). To balance trial counts between wave and non-wave conditions, in this analysis we used the median of the $\rho_{\varphi,d}$ distributions as the wave-detection threshold. We then fit a sinusoid by least-squares estimate to the binned conditional probabilities in wave and non-wave states. Finally, significance of the difference in modulation amplitude between the two states was assessed in each monkey by comparing confidence intervals for each fit at the $\alpha = 0.05$ level.

Data availability

The data that support the findings of this study are available from the corresponding authors upon reasonable request. Source data are provided with this paper.

Code availability

An open-source code repository for all methods is available on GitHub: http://mullerlab.github.io.

48. Gabor, D. Theory of communication. Part 1: The analysis of information. *J. Inst. Electr. Eng. 3* **93**, 429–441 (1946).
49. Le Van Quyen, M. et al. Comparison of Hilbert transform and wavelet methods for the analysis of neuronal synchrony. *J. Neurosci. Methods* **111**, 83–98 (2001).
50. Oppenheim, A. V., Schafer, R. W. & Buck, J. R. *Discrete-Time Signal Processing*. (Prentice Hall, 1999).
51. Marple, L. Computing the discrete-time analytic signal via FFT. *IEEE Trans. Signal Process.* **47**, 2600–2603 (1999).
52. Johansson, M. *The Hilbert transform*. Masters Thesis. Växjö University (1999); http://www.fuchs-braun.com/media/d9140c7b3d5004fbffff8007fffffff0.pdf
53. Feldman, M. Hilbert transform in vibration analysis. *Mech. Syst. Signal Process.* **25**, 735–802 (2011).
54. Pereda, E., Gamundi, A., Rial, R. & González, J. Non-linear behaviour of human EEG: fractal exponent versus correlation dimension in awake and sleep stages. *Neurosci. Lett.* **250**, 91–94 (1998).
55. Linkenkaer-Hansen, K., Nikouline, V. V., Palva, J. M. & Ilmoniemi, R. J. Long-range temporal correlations and scaling behavior in brain oscillations. *J. Neurosci.* **21**, 1370–1377 (2001).
56. Milstein, J., Mormann, F., Fried, I. & Koch, C. Neuronal shot noise and Brownian 1/f2 behavior in the local field potential. *PLoS ONE* **4**, e4338 (2009).
57. Rao Jammalamadaka, S. & Sengupta, A. *Topics in Circular Statistics* (World Scientific, 2001).
58. Rosa, M. G. P. & Elston, G. N. Visuotopic organisation and neuronal response selectivity for direction of motion in visual areas of the caudal temporal lobe of the marmoset monkey (*Callithrix jacchus*): middle temporal area, middle temporal crescent, and surrounding cortex. *J. Comp. Neurol.* **393**, 505–527 (1998).
59. Frank, T. D. & Richardson, M. J. On a test statistic for the Kuramoto order parameter of synchronization: An illustration for group synchronization during rocking chairs. *Physica D* **239**, 2084–2092 (2010).
60. Menard, S. *Applied Logistic Regression Analysis* (Sage, 2002).
61. Menard, S. Six approaches to calculating standardized logistic regression coefficients. *Am. Stat.* **58**, 218–223 (2004).
62. Tehovnik, E. J., Slocum, W. M., Carvey, C. E. & Schiller, P. H. Phosphene induction and the generation of saccadic eye movements by striate cortex. *J. Neurophysiol.* **93**, 1–19 (2005).
63. Bremmer, F., Kubischik, M., Hoffmann, K.-P. & Krekelberg, B. Neural dynamics of saccadic suppression. *J. Neurosci.* **29**, 12374–12383 (2009).

Author contributions Conceptualization: Z.W.D., L.M., J.H.R.; data curation: Z.W.D., L.M.; formal analysis: Z.W.D., L.M.; funding acquisition: Z.W.D., L.M., T.S., J.H.R.; investigation: Z.W.D., L.M.; methodology: Z.W.D., L.M., T.S., J.M.-T., J.H.R.; supervision: T.S., J.M.-T., J.H.R.; visualization: Z.W.D., L.M.; writing original draft: Z.W.D., L.M., J.H.R.; and writing, review and editing: Z.W.D., L.M., T.S., J.M.-T. and J.H.R.
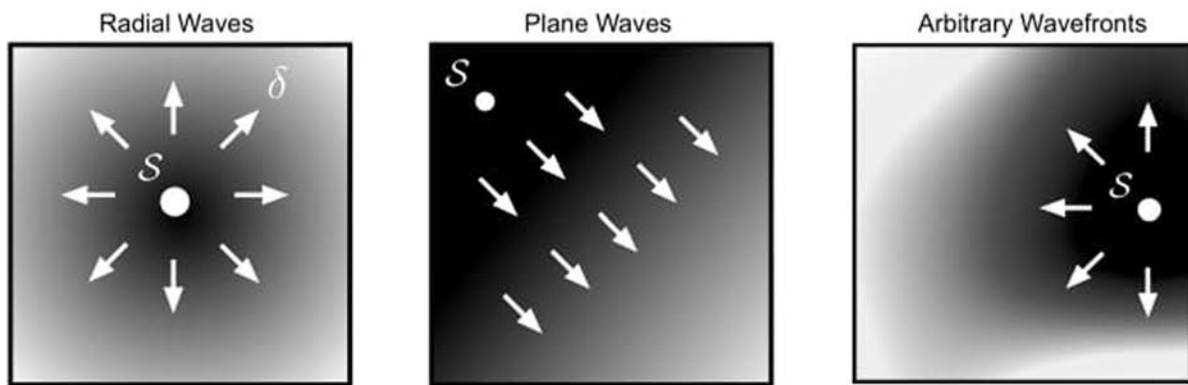
Article
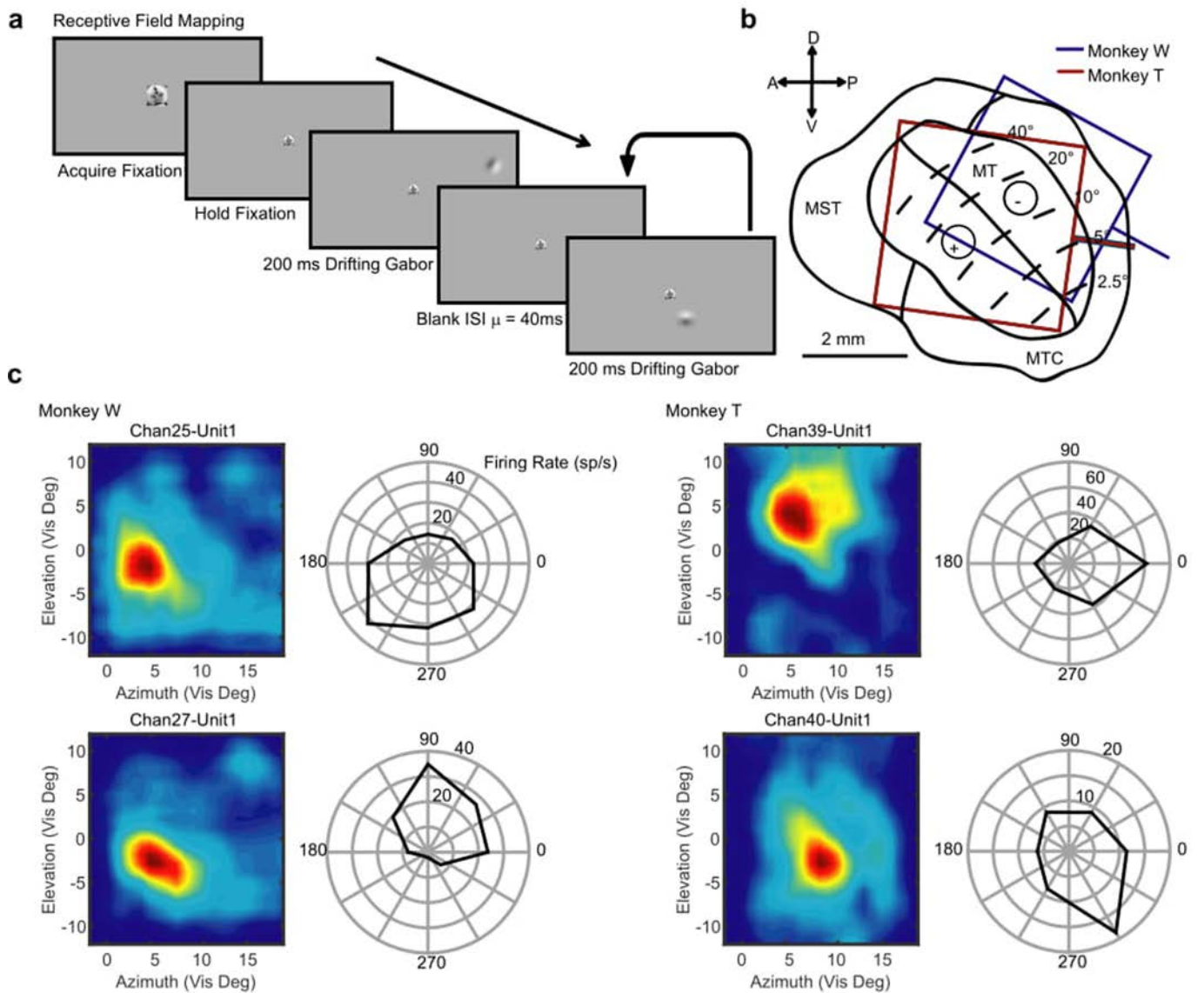
Extended Data Fig. 1 | Retinotopic mapping and motion direction tuning is consistent with the anatomical organization and tuning preferences of marmoset MT. a, Receptive fields for recorded units were measured by reverse correlation. Monkeys held fixation on a marmoset face while visual probes (drifting Gabor) appeared at random locations in the visual hemifield contralateral to the recording array. Each probe would appear, drift for 200 ms, and disappear after which a new probe would appear in a new random location and the process would repeat until the monkey broke fixation. **b**, The estimated position and orientation of Utah arrays in area MT based on retinotopy and histological examination for monkey W (blue) and monkey T (red). **c**, Example receptive fields and their preference for motion direction were consistent with previous reports of marmoset MT[58].
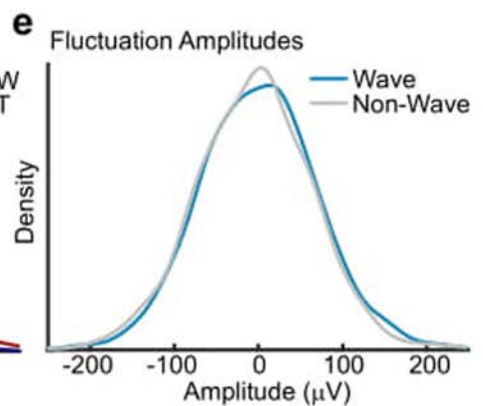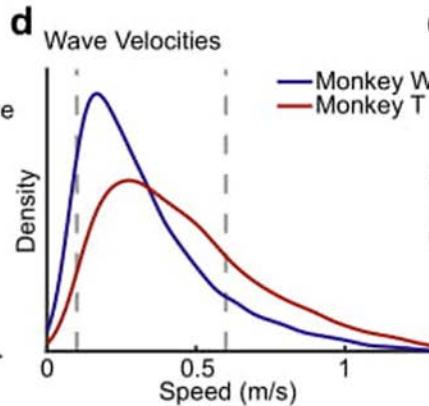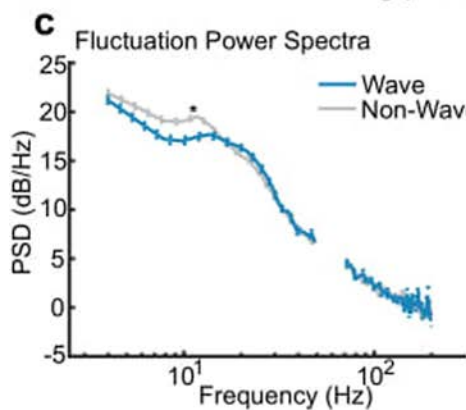
a

Step 1: Find the most likely starting point for a wave

start with "generalized phase" representation

$\phi_{x,y,t}$

y t x

$\nabla \cdot \nabla \phi$

$\underbrace{d_{x,y,t}}$ divergence field (captures flow from each point on electrode array)

$\underset{x,y}{\arg\max}\, d_{x,y,t}$

$\underbrace{\mathcal{S}}$ putative source (x,y) at each time point
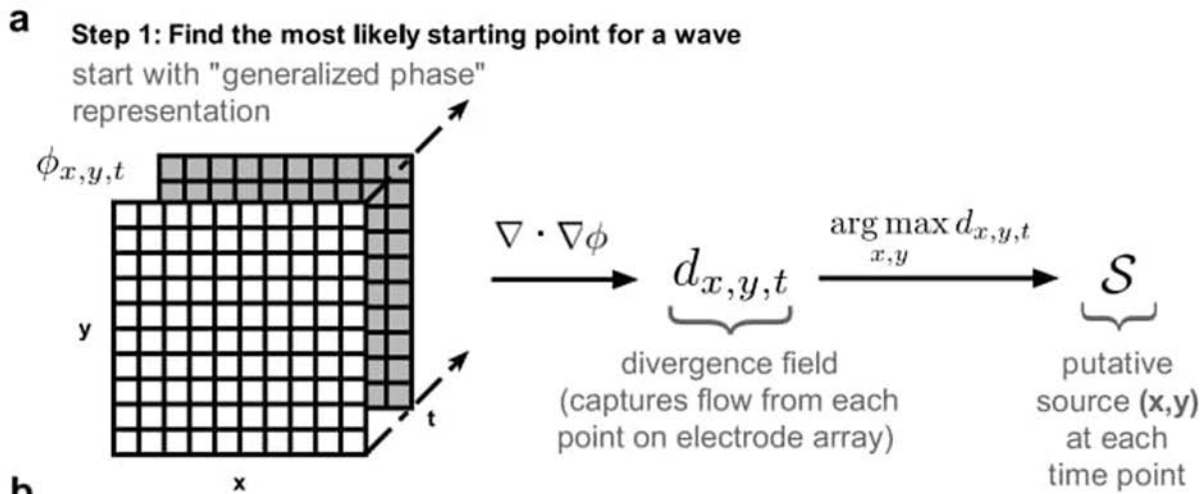
b

Step 2: Test for a wave traveling from this starting point

Radial Waves   Plane Waves   Arbitrary Wavefronts

$\mathcal{S}$ isolated starting point

δ distance in cortex from the isolated starting point

$\rho_{\phi,\delta}$ circular-linear correlation between generalized phase and distance from center point

c Fluctuation Power Spectra

PSD (dB/Hz) vs Frequency (Hz) — Wave / Non-Wave

d Wave Velocities

Density vs Speed (m/s) — Monkey W / Monkey T

e Fluctuation Amplitudes

Density vs Amplitude (μV) — Wave / Non-Wave

Extended Data Fig. 2 | Detection of spontaneous travelling waves. a, The method for detecting spontaneous waves from the Generalized Phase. First, the detection algorithm found the most likely starting point for a putative wave as the point that maximizes the divergence of the phase gradient (step 1). **b**, With this source point found, the algorithm then quantified the spatiotemporal organization about this point from the circular-linear correlation of phase with distance across the whole array (step 2). With this approach, the algorithm can robustly detect arbitrarily shaped wavefronts in the array data. **c**, The average power spectrum for waves ($N = 215$) had significantly less power in low

frequencies (<12 Hz) as compared to non-wave fluctuations ($N = 524$). Dotted bounds represent s.e.m. Asterisk: $P < 1 \times 10^{-5}$, two-tailed Wilcoxon rank-sum test. **d**, Detected waves in both monkeys predominantly travelled at speeds consistent with the conduction velocity of unmyelinated horizontal axons (0.1–0.6 m/s, red dashed lines; monkey W, 5571 waves, blue line; monkey T, 9285 waves, red line). **e**, There was no difference in the amplitude of fluctuations that were detected as waves (blue line; $N = 696$ waves) or rejected (non-wave, grey line; $N = 565$ non-wave fluctuations; example monkey T session).

Article
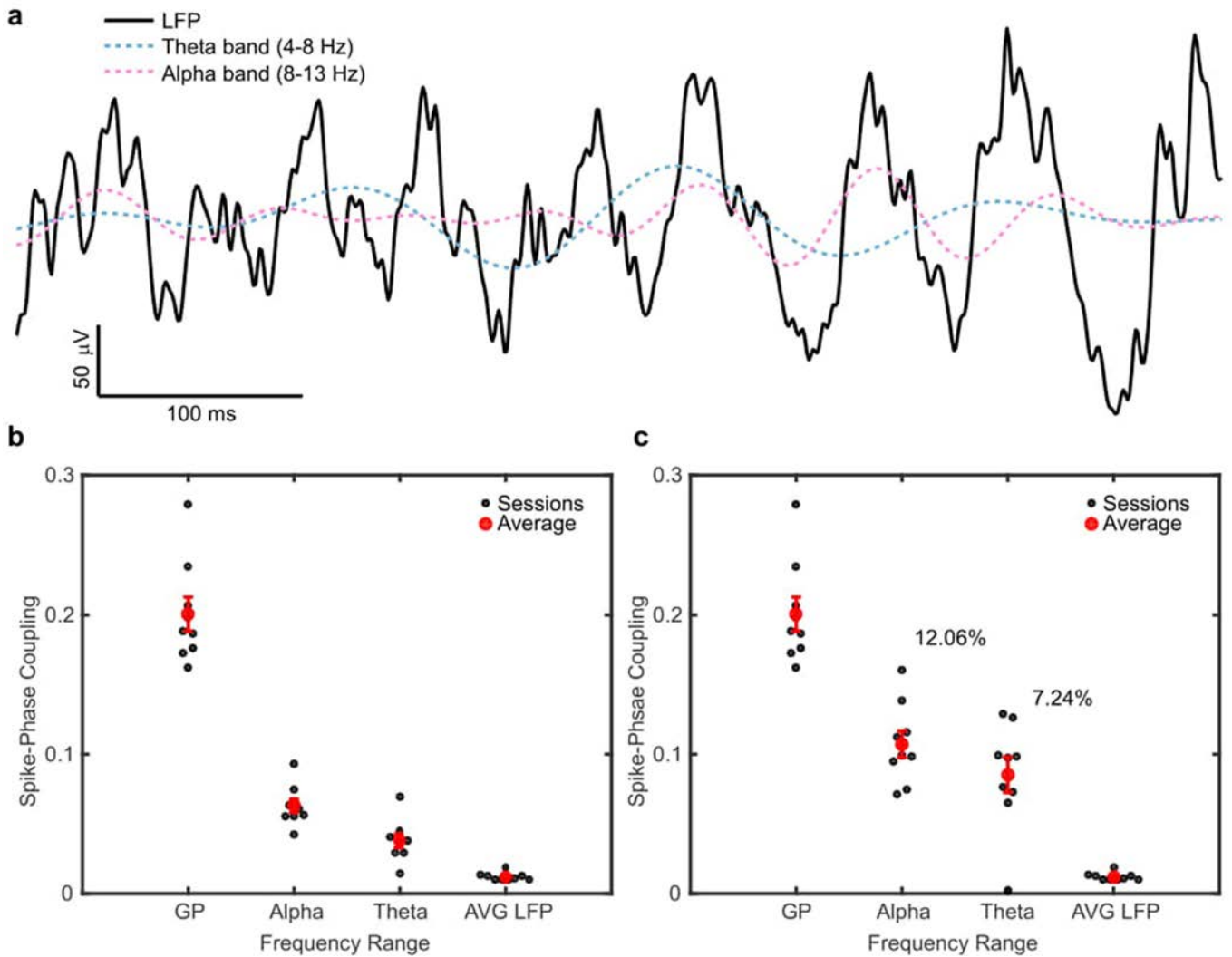
Extended Data Fig. 3 | Wideband GP is better coupled to spike timing than narrowband alpha or theta filters. a, The phase and amplitude of the raw (5–100 Hz) LFP was poorly captured by narrow-band theta (4–8 Hz, blue dotted line) or alpha (8–13 Hz, red dotted line) filters. **b**, Scatter plot showing spontaneous spike-phase coupling was greater for GP (5–40 Hz) than alpha or theta narrowband filtered phases. Coupling averaged across electrodes for individual recording sessions is plotted as black dots and each red dot represents the average value across sessions. **c**, Spontaneous spike-phase coupling remained stronger for GP than the narrow frequency bands even when the spontaneous LFP epochs were restricted to periods where there is large alpha (12.06% of recorded time) or theta (7.24%) LFP power during fixation (5 dB SNR, narrow- to broad-band power ratio). Results are presented from monkey W.
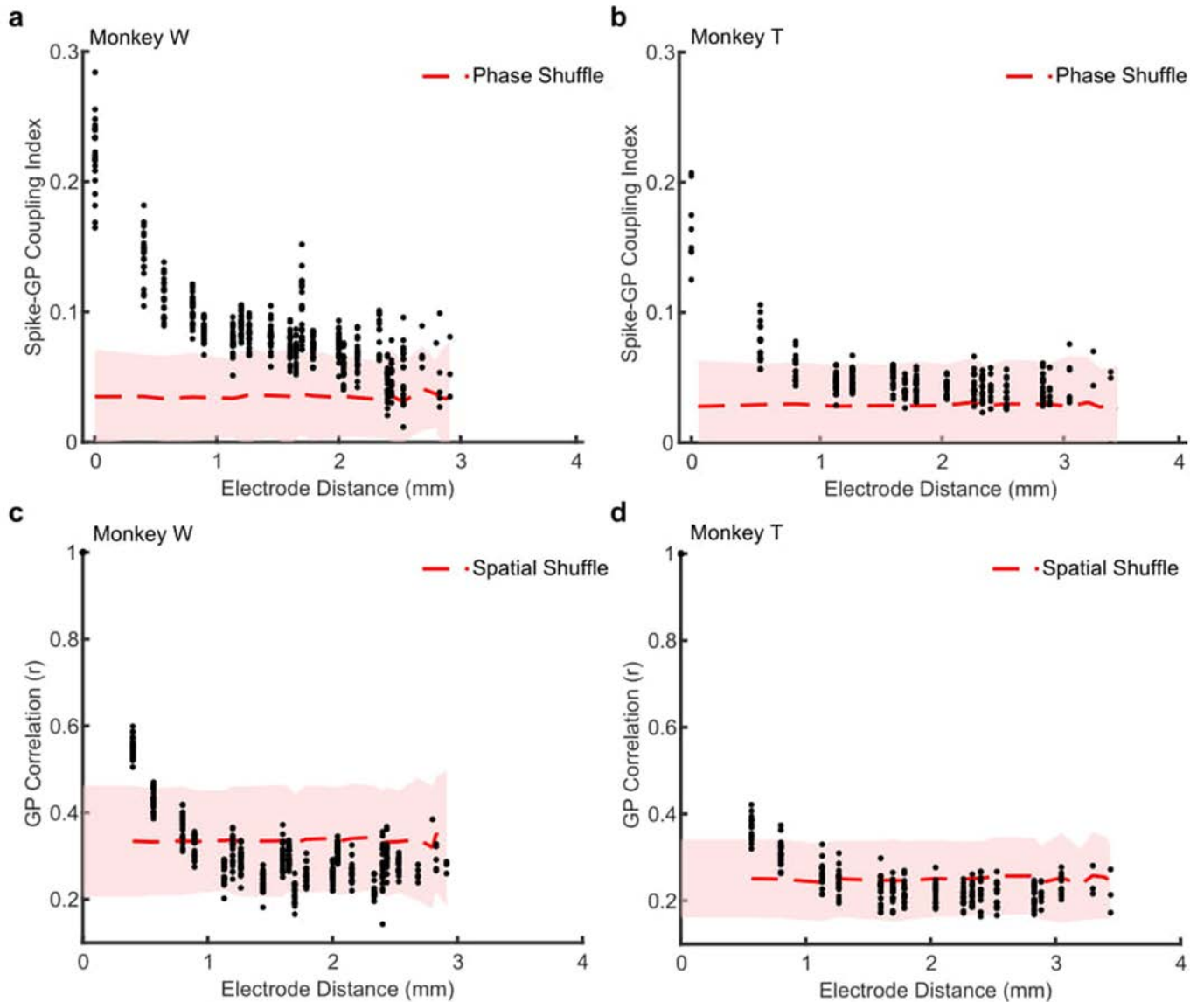
**Extended Data Fig. 4 | Spike coupling to GP is spatially dependent.**
a, Scatter plot showing the average spike–GP coupling across the distances of the array. Each point was averaged across a given spike-phase distance for a single recording session in monkey W (*N* = 22 sessions). The red dashed line shows the average null distribution for shuffled phases ± 2 s.d. (shaded region). **b**, Same as **a**, but for monkey T (*N* = 18 sessions). **c**, Scatter plot showing the cross-channel GP correlation for 200 ms of LFP during fixation across the electrode distances of the recording array. Each dot is the average circular correlation within an individual recording session across that channel distance. Shaded region represents the mean (±2 s.d.) correlation after shuffling the spatial position of the electrodes. **d**, Same as **c**, but for monkey T.
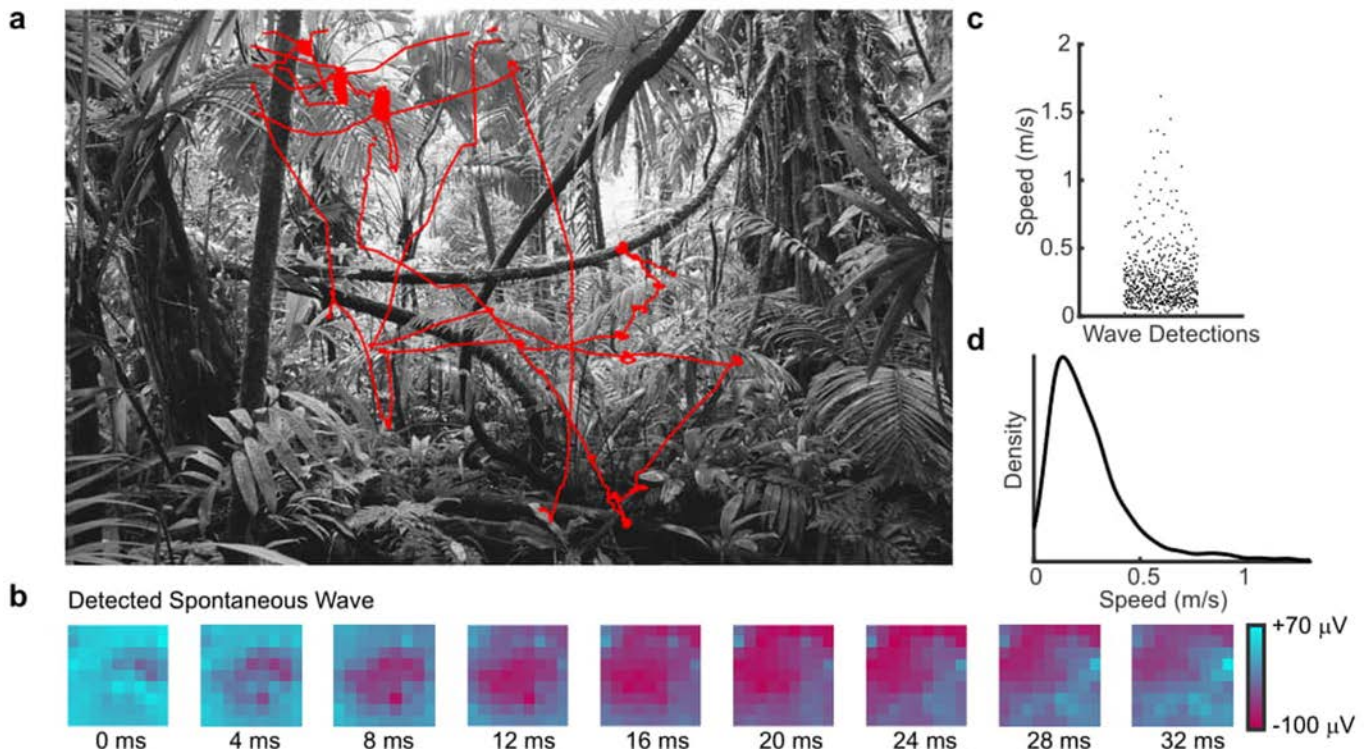
Extended Data Fig. 5 | Spontaneous travelling waves are present during normal viewing of naturalistic visual scenes. Marmosets freely viewed static natural images for 10 s while head-fixed. **a**, An example high-contrast image with the gaze of the marmoset over the 10 s viewing interval shown in red. **b**, An example of a spontaneous travelling wave detected during a period of fixation while monkey T was freely viewing a high-contrast image. **c**, Across 86 trials, 593 spontaneous travelling waves were detected during spontaneous fixations while the monkey freely viewed the images (−50 to +100 ms perisaccadic activity excluded). **d**, The density of observed wave speeds was consistent with the conduction velocity of unmyelinated axons (0.1–0.6 m s^{-1}).
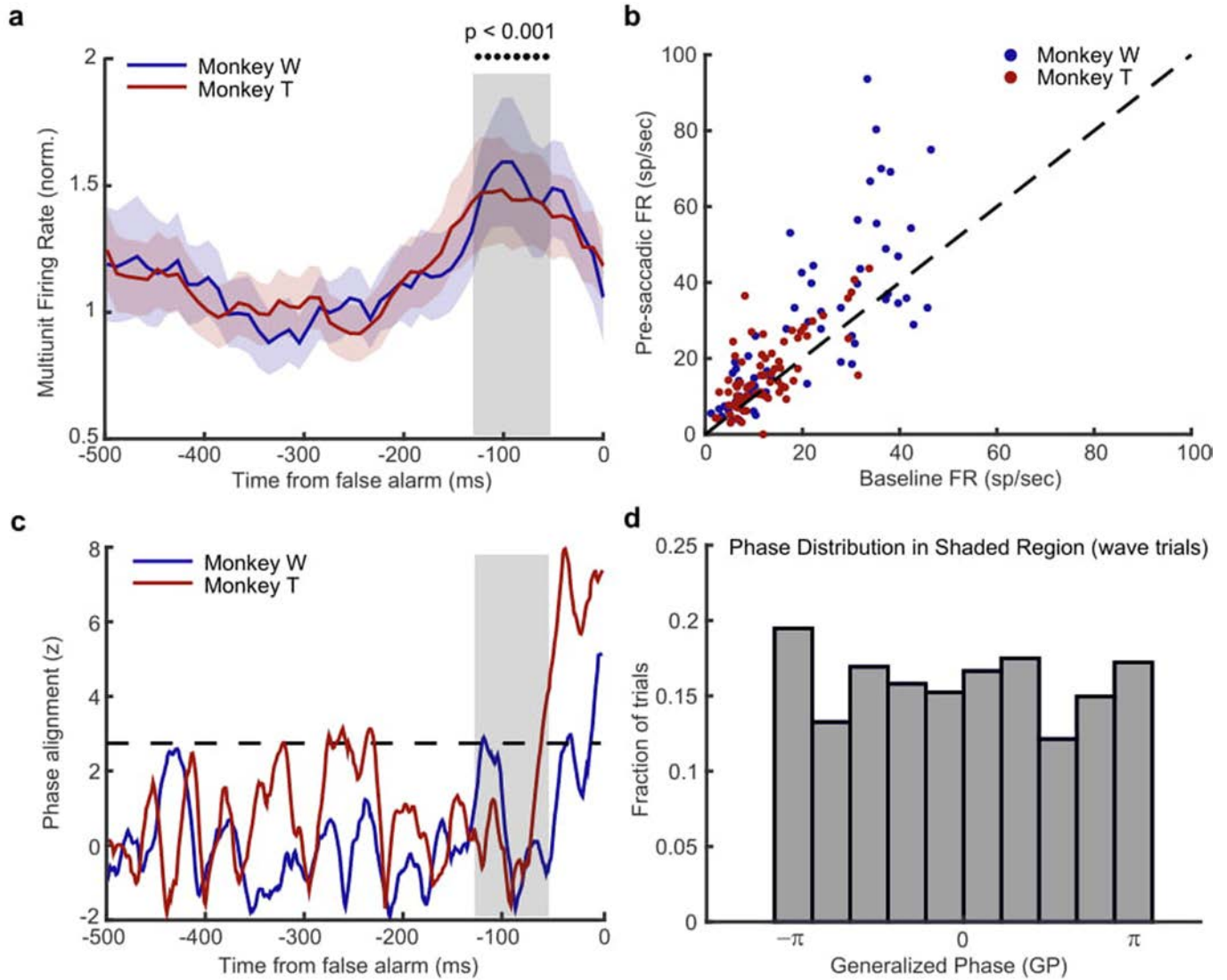
Extended Data Fig. 6 | False alarms are not predicted by the phase of travelling waves. To test whether the alignment of waves with the target location produces a bias towards saccading to that location, we examined the spontaneous activity before false alarms, time locked to the eye movement. This is distinct from our analysis of hits, which was time locked to the onset of the target, and is a limitation in our design for comparing hits to false alarms. However, we did find a significant modulation of spontaneous spiking activity that was possibly the sensory signal generating the false alarm, giving us a window to explore their potential relationship with waves[62]. If waves increase the likelihood of false alarms, they should show some phase-dependent relationship similar to what we observe in hits, but time-locked to the spiking activity predictive of a false alarm. **a**, Multi-unit spiking activity (normalized to the baseline, shaded regions ± s.e.m.) for monkey W (blue) and monkey T (red) was significantly increased in the interval before a false alarm (grey shaded box, −120 ms to −60 ms, $P < 0.001$, two-sided Wilcoxon rank-sum test). **b**, Scatter plot showing the average firing rate before the false alarm (*y* axis, shaded interval in **a**) was significantly greater than the spontaneous

background firing rate (*x* axis, −400 ms to −200 ms) for monkey W (blue dots; $N = 62$ multi-units, $P < 0.0001$, Wilcoxon signed rank test) and monkey T (red dots; $N = 70$ multi-units). **c**, Cross-trial phase alignments for waves aligned to the location of false alarm for the interval preceding the occurrence of a false alarm. There was no strong phase alignment during the period of significant spiking activity (shaded region) for either monkey W (blue line) or monkey T (red line) that would show a wave state is predictive of a false alarm. However, there was a strong phase alignment just before (monkey T −40 ms) and during the eye movement (monkey W, 0 ms). Given their close proximity to the onset of the eye movement we suspect the observed alignment may reflect an efference signal related to the pending saccade[63]. **d**, The distribution of observed wave phases was uniform during the period of significantly increased spiking activity (−90 ms before false alarm), indicating there was no relationship between the phase of spontaneous waves and the spontaneous spiking fluctuation associated with false alarms. Data collapsed across both monkeys as there was no difference in their distributions.
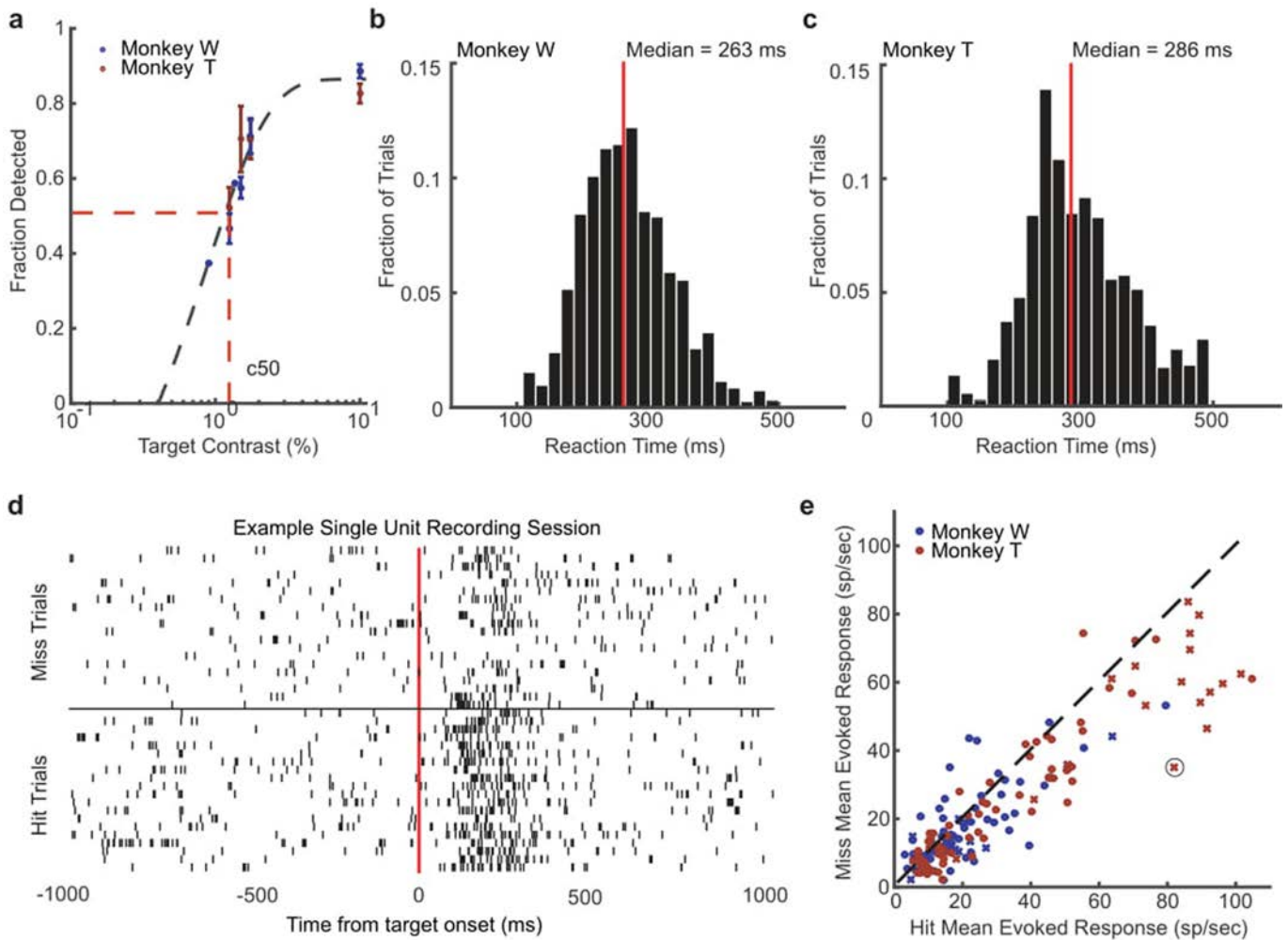
Extended Data Fig. 7 | Target-evoked response magnitude is correlated with detection performance. a, Detection performance of different target contrasts for monkey W (blue) and monkey T (red) across training days where those contrasts were presented. Both monkeys had similar psychophysical thresholds, defined as the contrast where the monkey detected the target 50 percent of the time on average (c50) as estimated from a sigmoid fit (grey dashed line). **b**, **c**, Distributions of reaction times for monkey W (**b**) and monkey T (**c**) during the detection task at their c50 value. The median reaction time for each monkey is shown by a red line. **d**, Spike rasters for an example neuron with trials sorted into hits (bottom rasters) and misses (top rasters). **e**, Scatter plot showing the distribution of mean hit (*x* axis) and miss (*y* axis) evoked responses (80–200 ms) for all single- (x) and multi-units (dot) recorded across all sessions for monkey W (blue) and monkey T (red). The circled x is the example neuron from **d**. Target-evoked responses were significantly stronger for detected targets in both monkeys. (monkey W, $N = 25$ single- and 83 multi-units, $P < 0.01$; monkey T, $N = 27$ single and 110 multi-units, $P < 1 \times 10^{-5}$; two-sided Wilcoxon signed-rank test).
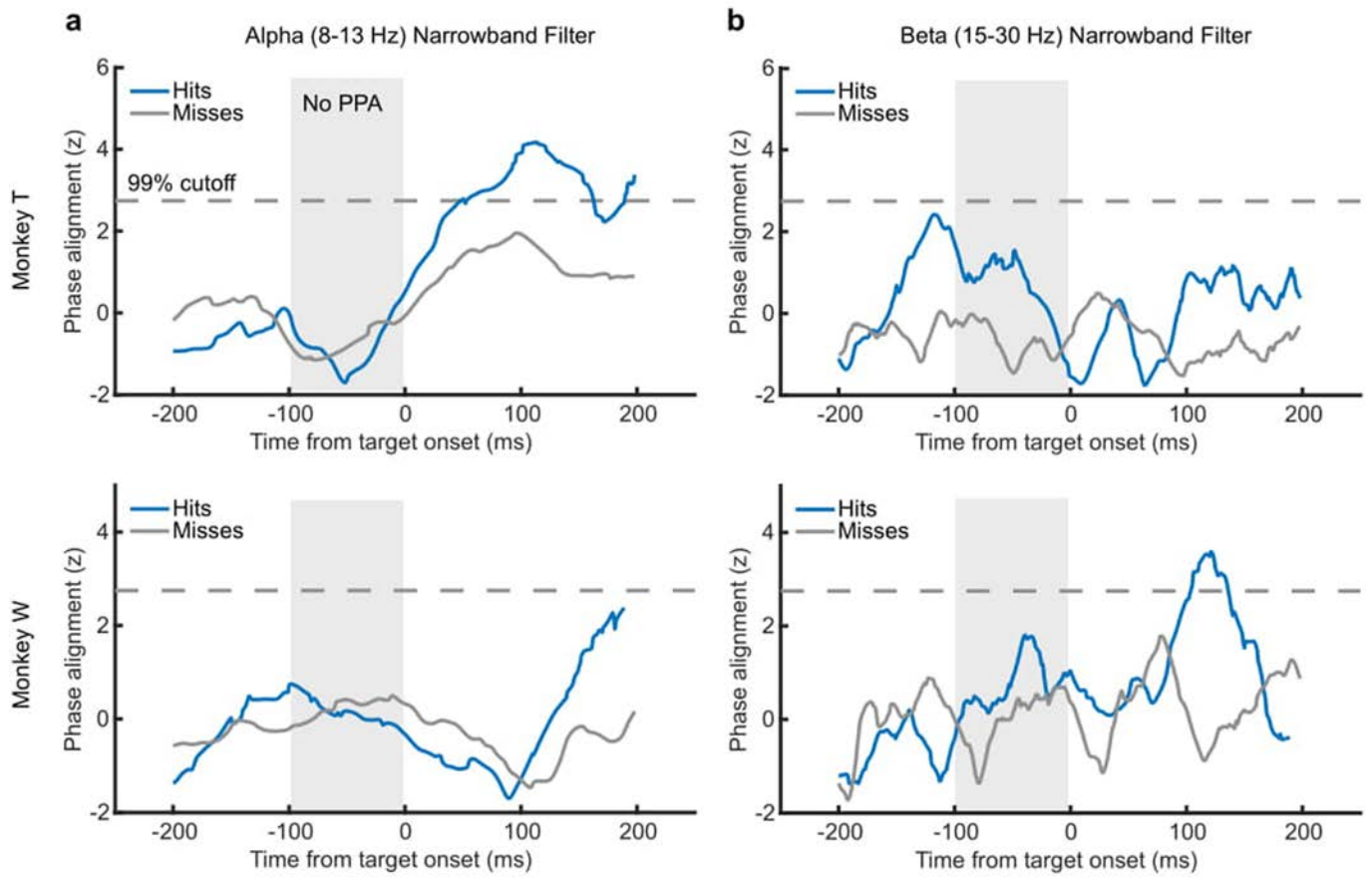
Extended Data Fig. 8 | Narrowband filters fail to detect any significant wave phase alignment before target onset. a, The cross-trial phase alignment computed as in Fig. 3, but using a narrowband alpha (8–13 Hz) filter, did not show any significant alignment (grey dashed line) for hits (blue) or misses (grey) before target onset (grey region) for either monkey T (top) or monkey W (bottom). **b**, The same as in **a**, but for a beta (15–30 Hz) narrowband filter.
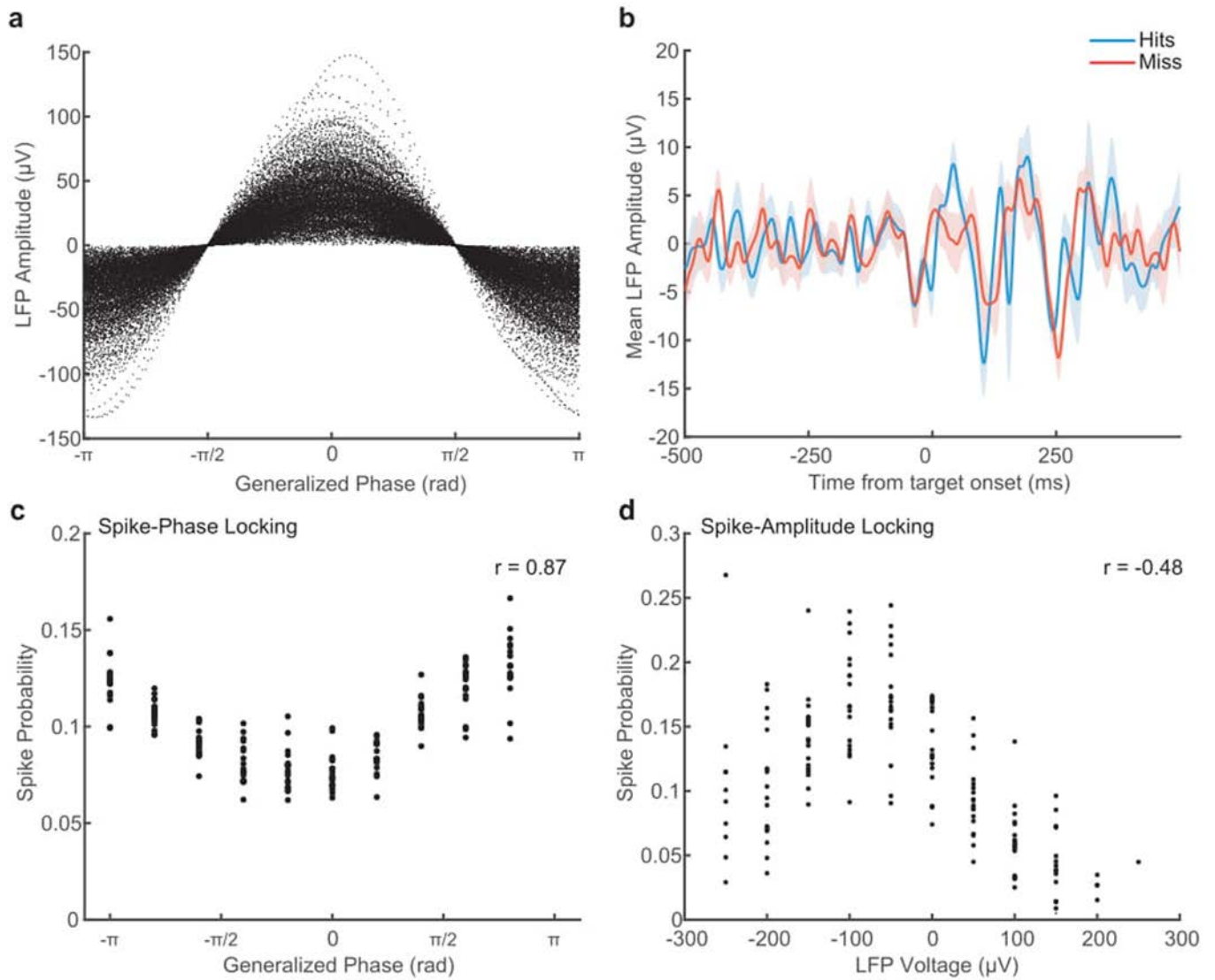
Extended Data Fig. 9 | Instantaneous voltage is less predictive of spike timing and perception than GP. a, Scatter plot showing the relationship between instantaneous LFP amplitude in voltage, and GP. The same voltage value occurred across a broad range of phases. **b**, While we found wave phase to be predictive of detection, the average LFP voltage was not different preceding a hit (blue) or a miss (red). Shaded area indicates s.e.m. across 18 sessions in monkey T. **c**, Scatter plot showing the coupling of spike probability to GP. Each point is the probability of a spike occurring in that phase bin within a recording session ($N=18$). There was a strong circular-linear correlation of GP with spike probability ($r=0.87$). **d**, Scatter plot showing weaker spike-amplitude coupling. Each point is the relative probability of a spike occurring in each voltage bin, normalized by the amount of time that instantaneous voltage occurs. Spike probability was less correlated with LFP amplitude (Spearman's rank correlation, $r=-0.48$).